

See discussions, stats, and author profiles for this publication at: <https://www.researchgate.net/publication/222090294>

Precise Chemical, Electronic, and Magnetic Structure of Binuclear Complexes Studied by Means of X-ray Spectroscopies and Theoretical Methods

ARTICLE *in* THE JOURNAL OF PHYSICAL CHEMISTRY C · NOVEMBER 2011

Impact Factor: 4.77 · DOI: 10.1021/jp2069804

CITATIONS

2

READS

41

11 AUTHORS, INCLUDING:



Karsten Kuepper

Universität Osnabrück

77 PUBLICATIONS 621 CITATIONS

[SEE PROFILE](#)



David Benoit

University of Hull

47 PUBLICATIONS 670 CITATIONS

[SEE PROFILE](#)



Ulf Wiedwald

University of Duisburg-Essen

70 PUBLICATIONS 1,044 CITATIONS

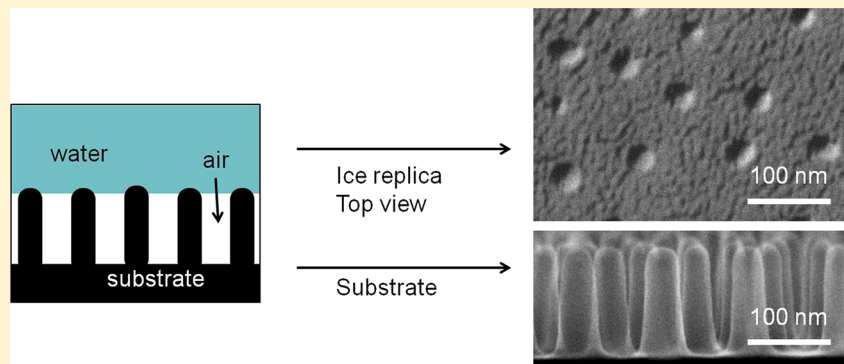
[SEE PROFILE](#)

Freeze Fracture Approach to Directly Visualize Wetting Transitions on Nanopatterned Superhydrophobic Silicon Surfaces: More than a Proof of Principle

Stefan Wiedemann,^{*,†} Alfred Plett[†], Paul Walther,[‡] and Paul Ziemann[†]

[†]Institute of Solid State Physics and [‡]Central Facility for Electron Microscopy, Ulm University, Ulm, Baden-Württemberg, Germany

 Supporting Information



ABSTRACT: Freeze fracturing is applied to make the wetting behavior of artificially nanopatterned Si surfaces directly visible. For this purpose, almost hexagonally arranged nanopillars of fixed areal density ($127 \mu\text{m}^{-2}$) and diameters (35 nm) but varying heights (40–150 nm) were fabricated on silicon. Measurement of contact angles (CAs) including hysteresis allowed to distinguish between the Wenzel (W) and the Cassie–Baxter (CB) states with droplets completely wetting the pillars or residing on top of them, respectively. Providing additional depth contrast by evaporating the ice replica with thin carbon and (typically 3 nm) platinum layers under 45° allowed resolving 3D features of 5 nm within the ice replica. In this way, laterally sharp transitions from CB- to W-states could be revealed, indicating the formation of zero-curvature water surfaces even on the nanoscale.

INTRODUCTION

Among the many phenomena resulting from topologically patterning surfaces on the micro- and/or nanoscale, superhydrophobicity is certainly one of the most popular. This type of wetting is often addressed as “Lotus-effect” due to the naturally occurring hydrophobic behavior of Lotus leaves causing their amazing ability of self-cleaning. Once the underlying combination of chemistry and surface roughness on the micro- and nanoscale had revealed,^{1,2} mimicking this principle has become a very active field of nanoscience.^{3–13} Examples of such artificial roughness are given by various arrays of lithographically prepared surface pillars with well-defined geometries and areal densities. Depending on geometrical parameters as well as on details of additional chemical coatings, hydrophobic (contact angle $\theta \geq 90^\circ$) or superhydrophobic ($\theta \geq 150^\circ$) surfaces can be obtained. For rough hydrophobic surfaces, quite generally two limiting cases are distinguished: The Wenzel (W-state)¹⁴ and the Cassie–Baxter regime (CB-state).¹⁵ Assuming artificially prepared surface pillars, in the W-state, a water droplet completely wets the surface including the bottom between the pillars. Since the effective wetted surface area A is enhanced relative to a smooth reference area A_0 due to the additional pillar walls, that is, $r = A/A_0 > 1$, the contact angle (CA) θ^W is related to the value of the smooth reference θ

by $\cos \theta^W = r \cos \theta$. In the CB-state, on the other hand, droplets reside on top of the pillars resulting in bags of air filling the volume in between the pillars. In this way, a three-phase contact line water–solid–air is formed on the pillars. With f describing the wetted area fraction, the CA values for the CB-state can be written as $\cos \theta^{CB} = f \cos \theta - 1 + f$. In this description, the simplification of a completely wetted flat top surface of all pillars is assumed. In reality, however, most pillars including those of the present work exhibit curved top surfaces. In that case, each pillar will penetrate into the water droplet to a depth allowing for the appropriate CA value. For the case of hemispherical capped cylindrical pillars one writes $\cos \theta^{CB(hs)} = f(\cos \theta + 1)^2 - 1$ with $f = f_{cylinder}$.¹⁶ It is exactly this penetration which will help us to localize our nanopillars and to distinguish the CB- from the W-state when applying the freeze fracture technique to analyze the lateral transition range between coexisting W- and CB-states which were observed in the present study.

The above introduced static contact angles do not yet consider hysteretic effects. Experimentally, however, different CA values are observed for a water droplet on top of a given

Received: August 31, 2012

Published: December 21, 2012



ACS Publications

© 2012 American Chemical Society

material depending on whether its volume is growing ("advancing CA", θ_{ad}) or decreasing ("receding CA", θ_{re}), thus giving rise to hysteresis. This plays an important role for experimentally distinguishing between W- and CB-states since the corresponding hysteretic behavior is found dramatically different: Huge hysteresis in the W-state (for the samples analyzed here, differences $\theta_{ad} - \theta_{re}$ up to 60° are observed) and small hysteresis in the CB-state.^{5–11} In most applications related to wetting, its dynamics appears decisive. Thus, control over the above two limiting states is of utmost importance. This immediately explains why a large number of studies are available analyzing the wetting behavior on surfaces with artificial arrays of various pillar shapes and distances fabricated by optical lithography on the micrometer scale.^{16–21} On this length scale, analysis is strongly supported by the applicability of optical microscopy revealing detailed information on CB- and W-states as well as on corresponding transitions.^{18–20} For instance, it has been found in this way that the CB- into W-state transitions of a water droplet occur over an extended length of many interpillar distances filling the subjacent air bags continuously.¹⁸ This observation immediately leads to the question whether such a laterally extended continuous transition is still possible if the diameters and the distances of and between surface pillars are all on the nanometer scale. Intuitively, that is not to be expected, since any partial transition invokes extreme local curvatures of the water surface between neighbored pillars corresponding to pressures and related energies making such a configuration highly improbable. Experimentally, however, this expectation has not been confirmed, yet. Since optical spectroscopies are no longer applicable, the few wetting experiments on nanoscaled arrays of pillars prepared by electron beam lithography (typical pillar dimensions 100 nm with distances of 300 nm or above)²² determine CA values for such patterned surfaces including their hysteretic behavior to identify in this way W- and CB-states, respectively. Such measurements, however, deliver only averages over the contact area of a droplet and no information is obtained on details of the three-phase contact line. Also, the effect of a local topological defect like a missing pillar on a CB- to W-state transition cannot be analyzed by applying hysteresis measurements. Rather, a high resolution visualization technique is necessary for that purpose. It is the aim of the present contribution to demonstrate that the method of freeze fracture in combination with scanning electron microscopy (SEM) is able to provide the required resolution. Freeze fracture is well established to extract structural information on various objects on the micrometer-scale especially in life science.^{8,23,24} It should be noted, however, that the usage of pure water for the freeze fracture method has found to be deteriorating resolution.⁸ This could be traced back to ice crystallization during slow freezing causing a significant increase of roughness.⁸ On the other hand, when applied to determine CA values on differently sized spherical colloids in contact with water/oil liquid interfaces, freeze fracture has recently demonstrated its ability to reveal features even on the nm-scale.²⁵

To the best of our knowledge the freeze fracture method has, however, not been applied previously to the above-mentioned questions related to the wetting behavior on the nanometer-scale with focus on possible CB- to W-transitions. To close that gap, presently nanopatterned Si surfaces are analyzed with respect to their wetting behavior by applying the freeze fracture method as well as CA hysteresis measurement. For that purpose, nearly hexagonally arranged arrays of Si nanopillars

were fabricated with geometrical parameters like pillar diameters and distances below 150 nm employing unconventional nanolithography based on self-organization of precursor loaded micelles and reactive ion etching (RIE). The results given below not only prove the applicability of freeze fracture to such fragile objects like Si nanopillars and confirm a resolution of better than 5 nm but also give new insights in the lateral sharpness of CB- to W-transitions on such surfaces.

MATERIALS AND METHODS

Sample Preparation. For nanopatterning of silicon surfaces (starting material: (001)-oriented commercial n-doped Si wafers), a two step process has been applied. First, an almost hexagonally arranged array of Au nanoparticles is prepared on top of the Si substrate exploiting the self-organization of precursor (HAuCl_4) loaded inverse spherical micelles formed by diblock copolymers [commercially available (Polymer Source Canada) poly(styrene)-block-poly(2-vinylpyridine); PS1850-b-P2VP900, numbers of monomers per block are added] in toluene used as a solvent. The details of the micellar technique are described elsewhere.²⁶ In the present context, it is worth noting that the diameters of the Au nanoparticles as well as their mutual distance (determined from SEM images applying imageJ-software) can be controlled with narrow corresponding distribution functions. In some cases, it is useful to further enhance the diameters of the primarily obtained Au nanoparticles. For that purpose, a recently developed electroless photoinduced selective growth process of Au on top of Au was applied.²⁷ The finally fabricated Au nanoparticles then serve as a mask during the subsequent reactive ion etching (RIE) with a mixture of CF_4 and CHF_3 . In this way, the diameter and areal density of the Au nanoparticles are transferred into the Si substrate while the height of the emerging Si nanopillars can be controlled by the etching time. More details can be found in ref 28. For the present application related to the wetting behavior of such nanopatterned surfaces, the finishing step consists of selectively removing residual Au masks by an I/KI-bath and coating the patterned surface with a Teflon-like layer. As will be demonstrated, in this way superhydrophobic Si surfaces are obtained as indicated by CA-values well above 150° . The complete fabrication procedure of such surfaces is schematically shown in Figure 1 together with SEM images giving examples of the outcome of the various intermediate steps.

Contact Angle Measurements. CA values were measured with a commercial OCA 15 Pro instrument (DataPhysics) providing an optical method to determine the shape of a water droplet (deionized water, $18.3 \text{ M}\Omega \text{ cm}$) in combination with a fitting procedure to extract the CA. Dosing of droplets is accomplished by using a syringe, allowing one to increase or decrease its volume at a flow rate of $0.5 \mu\text{L}/\text{s}$. Thus, advancing θ_{ad} and receding θ_{re} CAs are obtained, with typical errors in the range of 3° . Additional bouncing experiments were performed in order to distinguish static metastable CB-states from stable ones.²¹ For this purpose, the dosing syringe is retracted by 10 mm from the sample surface and droplets of $10 \mu\text{L}$ (radius 1.33 mm) are detached from it. In the present study on superhydrophobic surfaces, the falling droplets, when hitting the surface, bounce a number of times before finally coming to rest on the sample. By observing the bouncing droplets with a high speed camera (typically 400 frames per second), the number of rebounds and the related trajectories can be recorded. Finally, by taking CA hysteresis measurements on the resting droplet, one is able to decide whether it is still in the CB-state as in the static case without impacts. It turned out that increasing the starting height to 40 mm led to a burst of the droplet into smaller ones on surface impact. Thus, in all experiments on falling droplets the starting height was fixed to 10 mm (Supporting Information, S1).

Freeze Fracture in Combination with SEM. Applying freeze fracture in the present study related to superhydrophobic surfaces aims at replicas of three-phase interfaces solid–water–air with a resolution in three dimensions on the nanoscale. To reach that aim, the standard procedure of ref 8 had to be modified. First of all, rapid freezing of the

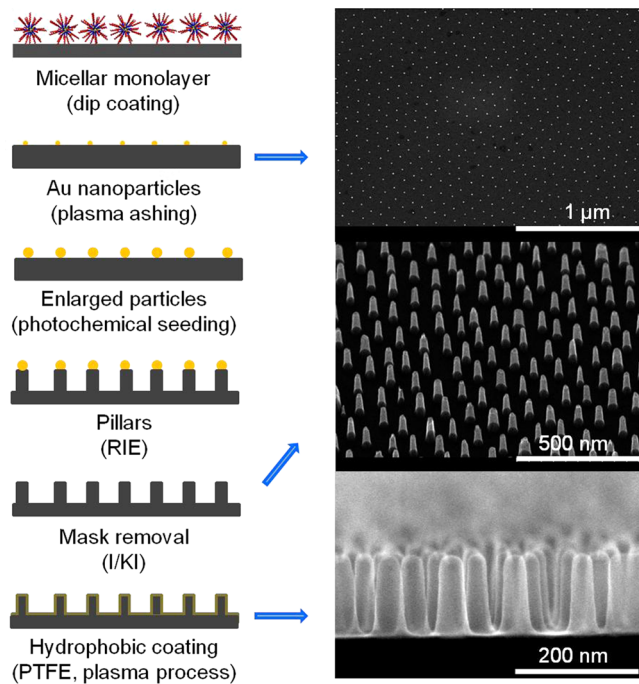


Figure 1. Left: Schematics of the sample preparation procedure. Right: Corresponding SEM-images as indicated by arrows. Top: Top view of micellar Au-nanoparticles with average value of diameters $d = 13$ nm and of distances $D = 93$ nm. Middle: 30° tilted SEM-image of Si-pillars after seeding and RIE etching. Bottom: Side view of final structure, $d = 35$ nm, $h = 130$ nm (pillar shapes are slightly conical and their tops almost hemispherical). Note different scale bars.

pure water is applied to avoid ice crystallization and, thus, the related roughening at the pillar–ice interface. Furthermore, after fracturing, the replica surface is coated by thin platinum and carbon layers. In more detail, a liquid droplet of deionized water is deposited into a cryo-SEM-holder and, next, the nanopatterned surface of a Si wafer is pressed onto that holder followed by shock-freezing the complete system in liquid propane at 77 K. Then the frozen system is transferred into an evaporation chamber (BAF 300, Balzers, Principality of Liechtenstein) with a cooling stage. The subsequent step is critical: Mechanical detachment of the substrate from the ice replica (“fracturing”) and, in parallel, evaporation of about 3 nm Pt and 5 nm carbon by electron beam evaporation onto the replica to avoid sublimation or readsorption of water and to stabilize the imprint. The added layers increase electrical conductivity, prevent charging, and, even more importantly, reduce effects of beam damage.²³ However, transfer of the cold replica from the evaporation chamber into the cryo-SEM apparatus (Hitachi S-5200; Hitachi, Tokyo, Japan) inevitably leads to additional water adsorption and, thus, ice formation. To remove that ice, the sample is carefully warmed up under vacuum within the SEM setup up to 156 K allowing for sublimation of the water condensed onto the sample during transfer.²³ Here, the Pt layer is of utmost importance allowing to separate transport-induced ice

from the replica. In the present experimental arrangement, the mass of the substrate is negligible compared to that of the sample holder. As a consequence, freezing front starts from the substrate and the formed ice replicates the topography of the original liquid surface. The essential steps of the freeze fracture method are summarized in the schematics presented in Figure 2. Images were obtained using a Hitachi S-5200 SEM instrument equipped with a Gatan cold stage 626 (Gatan, Inc., Pleasanton, CA) at an accelerating voltage of 10 kV, using the secondary electron detector, or the Autrata type backscattered electron detector. Though the electron interaction volume at 10 kV is in the range of 1 μm in ice, this does not necessarily limit the resolution, because there is much more electron scattering and therefore contrast generation in the overlaying 3 nm platinum layer than in the homogeneous bulk part of the ice. The BSE signal from the homogeneous ice and top carbon-coating is almost constant and therefore mainly adds statistical noise to the signal. Consequently, the Pt layer in combination with BSE tremendously improves depth resolution.²⁹ This advantage of the BSE mode as compared to standard SEM images is additionally demonstrated in the context of Figure 4 in the Supporting Information (cf. S3).

There is still another important experimental feature indicated in Figure 2: The Pt is evaporated at an angle of 45° relative to the replica surface. Thus, indentations in the ice replica are only partly covered by Pt producing bright SEM contrast while the shadowed parts appear dark. Knowing the diameter of the indentation as in our case given by the pillar geometry, allows calculating its depth from the determined size of the bright or dark area (cf. Figure 4 and Supporting Information S2). In this way, quantitative depth, that is, 3-D information is obtained.

RESULTS AND DISCUSSION

Since the freeze fracture experiments aimed at imaging three-phase interfaces, superhydrophobic surfaces were in the focus with stable CB-states. For that purpose, a series of nanopatterned Si surfaces were prepared at approximately identical distances between equally shaped slightly conical nanopillars (cf. Figure 1) while systematically varying their heights by variation of the etching time. After plasma depositing the nanopatterned surfaces with teflonlike coating ($\text{CA}_{\text{ad}} = 118^\circ$ on the flat reference surface, what is typical for flat teflonlike surfaces^{16,30}), the CA values were determined as a function of the pillar height. The results are presented in Figure 3.

Clearly, a pronounced transition of the wetting behavior can be observed at pillar heights of approximately 70 nm (vertical dashed line in Figure 3). Below that critical height a marked CA hysteresis with a width of 60° is observed typical of a W-state. At the critical pillar height, this hysteretic behavior collapses to a typical residual width of 10° and the CA values get independent of the pillar height at about 160° indicating superhydrophobic CB-states. Though the lines in Figure 3 just serve as guide to the eye, they were drawn according to the approximations given in the introduction. For example, for the W-state the roughness parameter can be expressed as $r = 1 + \alpha h$ with a parameter $\alpha = w d \pi$ (w , areal density of nanopillars; d ,

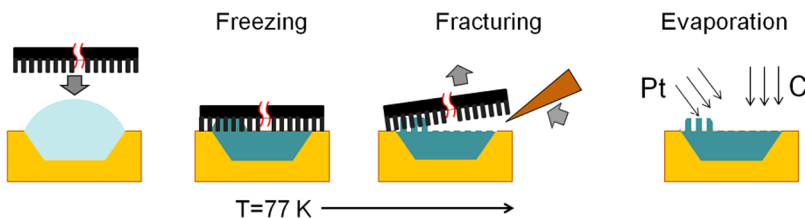


Figure 2. Schematics of the essential freeze fracture steps: Temporal sequence from left to right with the nanopatterned surface indicated by the comblike shape.

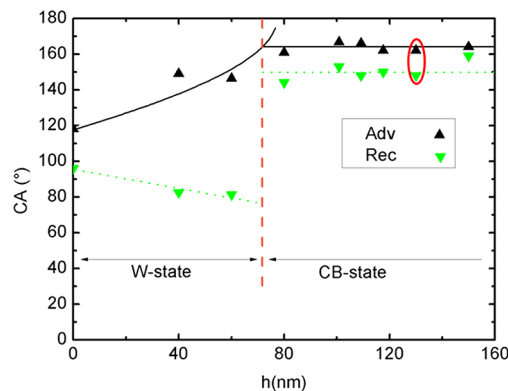


Figure 3. Advancing and receding contact angles (symbols defined in the inset, their size reflecting the related errors) as a function of pillar height of a nanopatterned Si surface, plasma coated with a PTFE-like coating (density of pillars $127 \mu\text{m}^{-2}$, average diameter 35 nm). The red encircling indicates the sample shown in Figure 1. Exactly this sample was chosen for freeze fracture. The vertical dashed line points to the collapse of the hysteresis by typically 60° at a well-defined pillar height. Other lines serve as a guide to the eye.

diameter of nanopillars; h , height of nanopillars). Additionally, the expected constant horizontal line for the CB-state can be calculated with $f = w\pi d^2/4$. The corresponding lines in Figure 3 were obtained with $\alpha = 0.014 \text{ nm}^{-1}$ and $f = 0.09$. Assuming perfect cylinders with smooth walls, from the experimentally determined geometries, one calculates $\alpha = 0.016 \text{ nm}^{-1}$ and $f = 0.12$ with a corresponding $\theta^{\text{CB}} = 159^\circ$ for cylinders. When assuming half-spherical caps on top of cylindrical pillars one receives for the CB-state $\theta^{\text{CB(hs)}} = \arccos(f(\cos \theta + 1)^2 - 1) = 165^\circ$. Here the formula for hemispherical caps fits slightly better what is also expected from the pillar shape (see Figure 1). These values are also comparable to the measurements reported in refs 16, 21, and 22.

In the present context, however, the data of Figure 3 form just the basis to guarantee that the sample used for the freeze fracture (pillar height 130 nm, encircled in Figure 3) is in CB-state under standard pressure conditions. To additionally corroborate the stability of the CB-state, water droplets falling 10 mm from above the nanopatterned superhydrophobic surface were analyzed. In case of the sample with 130 nm high pillars, the droplet showed 10 rebounds before coming to rest (cf. Supporting Information S1). In this final state, the droplet exhibited a narrow hysteresis width of 10° , proving that it was

still in the CB-state despite the additional effective pressure it experienced during the 10 impacts.

The principal applicability of freeze fracture and its high three-dimensional resolution is demonstrated by the SEM images (backscattered electrons imaged with a BSE-YAG ring detector) presented in Figure 4. There, clear indentations are visible in the Pt + C coated ice replica of a CB-state realized on top of a nanopatterned Si surface (encircled in Figure 3).

These indentations mark the positions of the nanopillars which are, on average, 93 nm apart, a distance easily resolved by the freeze fracture approach. Obviously, the tips of the nanopillars slightly penetrated the water even in the CB-state leading to the visible nanogrooves. One step further, in the right panel of Figure 4 representing a magnified view of the rectangular area as marked in the left panel, each indentation reveals a bright and a dark area due to evaporating the Pt coating under 45° . Simple geometrical considerations approximating the pillar tips as spherical calottes allow estimating the penetration depth into the water from these bright/shadowed areas. The resulting value of approximately 20 nm for the penetration depth is compatible with the matching CA requirement at that depth (cf. Supporting Information S2). This consistency of the depth estimate provides evidence that the freeze fracture depth resolution is well below 20 nm. Indeed, close inspection of the area in between the nanogrooves in the magnified image of Figure 4 and comparison to corresponding areas outside marked frame in the left panel indicates some deterioration and roughening of the Pt film during the additional zooming-in due to enhanced electron beam intensity. This effect may finally limit the obtainable lateral contrast resolution, which, in the present case, is estimated from the sharpness of the indentation periphery in the magnified image as 5 nm.

Next, the replica is inspected on a larger scale, and the results are presented in Figure 5. Surprisingly, two areas can clearly be distinguished representing different heights of ice or, originally, water. Thus, the lower area can be identified as replicating the CB-state as expected, while the upper area indicates the presence of a W-state at least in some fraction of the nanopatterned sample surface despite the proven stability of the CB-state even against falling droplets. Thus, one has to conclude that during the rapid freezing process when preparing the replica, locally high pressures are generated which enforce a transition from CB- to W-states. The underlying scenario is that, during rapid freezing, at some point water transforms into

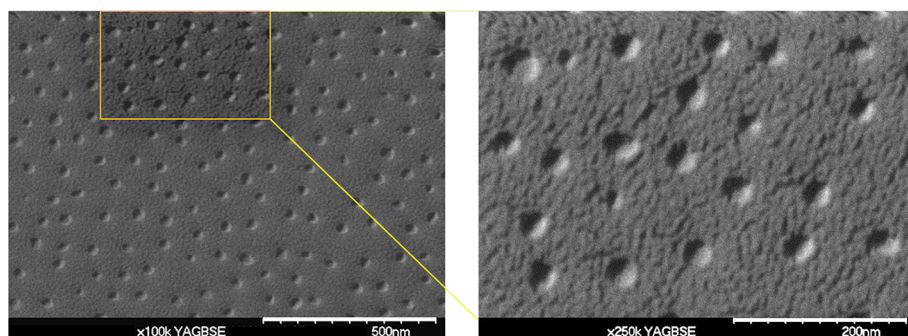


Figure 4. SEM images of a Pt + C coated ice replica obtained after applying freeze fracture to a superhydrophobic nanopatterned Si surface (encircled in Figure 3). Left panel: Overview with indentations demonstrating the slight penetration of the tips of nanopillars into the water droplet even in the CB-state. Right panel: Magnified view of the rectangular area marked in the left panel revealing a dark (evaporation shadow)-bright (Pt deposition) contrast due to the Pt deposition under 45° . This additional contrast delivers quantitative depth information.

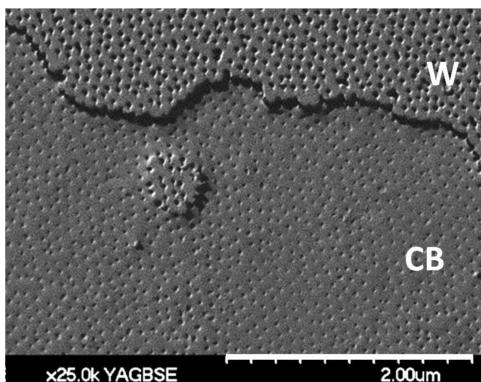


Figure 5. Image of freeze fracture replica taken by BSE mode on the same sample as in Figure 4, however on a larger scale. The visible height differences prove the simultaneous presence of W- and CB-states as indicated.

ice accompanied by a volume increase. This triggers a shock wave spreading through water at the speed of sound (1497 m/s) being much faster than the velocity of the freezing front (ca. 0.1 m/s, ref 31). Though the related additional pressure caused by a shock-wave can be principally estimated as $p_{\text{WH}} = K\rho c\Delta v$ (so-called water-hammer pressure, ρ = density of water and c = sound velocity in water), quantitative estimates are doubtful due to the strongly geometry dependent proportionality constant K which varies in the literature over at least 2 orders of magnitude for impinging droplets.^{29,32} For $K = 0.1$ and $\Delta v = 0.1$ m/s, one obtains 15 kPa as the lower limit. Independent of the detailed scenario, however, the experimental observation of coexisting CB- and W-states reveals the essential fact that the wetting states imaged by the replica are not necessarily those existing under equilibrium standard conditions.

On the other hand, the frozen-in states visible in Figure 5 deliver additional insight in two more respects: First, the small W-“island” enclosed by the CB-state approximately in the center of Figure 5 suggests the stability of local W-states against propagation. This is in agreement with a condition reported in¹⁸ according to which the ratio of pillar height to distance between pillars should obey $h/a > 0.6$ for advancing CA value of $\theta_{\text{ad}} = 118^\circ$ on a flat substrate as in the present case. For the surface delivering Figure 5, the ratio is $h/a = 2$ and, thus, the above blocking criterion is well fulfilled. This argument assumes that the water in the surrounding CB-state is still not frozen. Furthermore, the presence of local enhanced pressures due to shock waves induced during the rapid freezing process should favor further extension of small W-islands. Thus, the observation of such islands rather indicates that at the moment of their creation the surrounding water in CB-state had already transformed into ice. Though this point cannot clearly be unravelled, the coexistence of CB- and W-states as made visible by the freeze fracture method with high lateral resolution reveals sharp borderlines between these states. The lateral extension of the CB- to W-state is down to only one pillar distance, that is, below 100 nm. This immediately translates into correspondingly high curvatures at the water/air interfaces with related high local pressures. Thus, to account for such sharp boundaries, one has to assume local water/air interfaces forming saddle-shaped surfaces of average zero curvature. The present observation is in marked contrast to what has been reported for the corresponding case on the micrometer-scale.

There, the CB- to W-state for Laplace-pressure induced transitions were extending over several pillar distances.¹⁷

Finally, the role of defects in the nanopatterned surface for inducing CB- to W-state transitions will be addressed in the following. A special type of defect in the present case is a single missing nanopillar. Since it was demonstrated above that the lateral transition between such states extends just over one pillar distance, it might similarly be expected that a missing nanopillar will trigger a local instability of a CB-state. To test this experimentally, the same replica as in Figures 4 and 5 was screened for corresponding defects and two interesting locations are encircled in Figure 6.

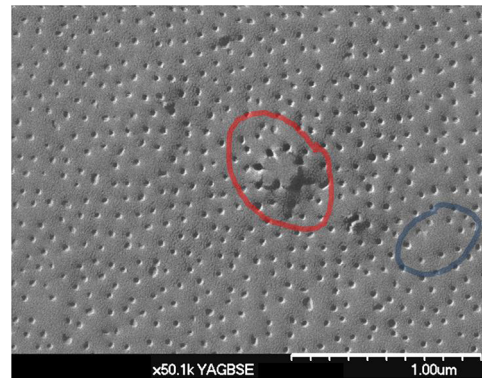


Figure 6. Image of freeze fracture replica (same as in Figures 4 and 5) taken by BSE mode revealing an area with two local defects as encircled. In both cases, a single nanopillar is missing. However, at the left, a transition into the W-state was induced while, at the right, the CB-state remained stable during freezing.

Closer inspection of the indentations suggests that in both cases probably one single nanopillar is missing. Nevertheless, these identical defects resulted in an opposite local wetting behavior: Transition into a W-state at the left, while conserving the CB-state at the right. Presumably, the local conditions during the very freezing decide which state will be stable. However, if formed locally, the W-state appears to be stable and not further spreading in accordance with the h/a -criterion given above.

Another special type of “defect” is formed by the boundary between the unpatterned area of the sample surface and its nanopatterned part with nanopillars. The result obtained on a similar sample as above is given in Figure 7a by presenting a SEM image of the ice replica containing such a boundary (cf. schematics of the sample and sample holder on the left of Figure 7a together with a topview SEM image of such a boundary from the same sample taken before freeze-fracturing (panel (b)). The ice replica clearly reveals an approximately 1 μm broad stripe parallel to the borderline to the unpatterned surface which is in W-state followed by the expected CB-state within the interior of the visible area (again the dark/bright contrast at pillar positions allows a clear identification of the border W-CB-regime). Comparison to panel (b) immediately suggests a correlation of the lateral extent of the W-state with a reduced areal density of the nanopillars starting from the very borderline toward the interior of the nanostructured area. This density gradient is intrinsically related to the dip coating technique applied for the deposition of micelles from their solution. It should be noted, however, that even the reduced areal pillar density delivers a ratio $h/a < 0.6$; that is, lateral

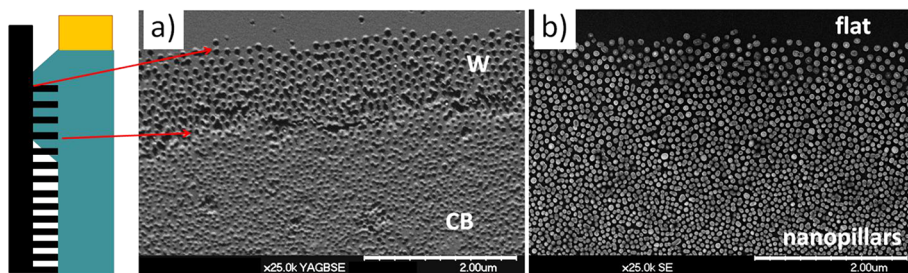


Figure 7. (a) Image of freeze fracture replica (here a 10%-water-glycerol-mixture was used) taken by BSE mode (left) with focus on the transition from an unpatterned to nanopatterned area (cf. scheme on the left). Despite that the nanopatterned surface exhibits a CB-state in equilibrium, the replica reveals a 1 μm broad stripe parallel to the borderline in the W-state. (b) Top view image of a corresponding but not identical sample area with increasing pillar density and decreasing interpillar distance in the first few micrometers.

spreading of the water between the nanopillars should be blocked. Opposite to this expectation, the observed W-state within the first micrometer again indicates the presence of a significant additional pressure during the rapid freezing process, at least sufficient to trigger water propagation into the less dense pillar arrangement close to their boundary. Though the details of that propagation are not clear, yet, it is worth noting that such a scenario of shock-wave induced wetting transitions have been reported previously.^{30,32} Alternatively, capillary-wave induced wetting transitions have been suggested.⁶ In the present study, nanopillars as short as 80 nm were sustaining the CB-state even after falling onto the surface from a height of 1 cm. Images of the bouncing droplet taken with a high speed camera (cf. Supporting Information S1B) demonstrate their vibrational excitation. Nevertheless, after these vibrations are completely damped out, the droplets are still in the CB-state as proven by additional hysteresis measurements. Thus, for the presently observed W-states, the capillary-wave mechanism can be excluded as mainly causing their existence.

CONCLUSION

Methodically, the present work provided clear first time evidence that the wetting behavior of pure water in contact with even such fragile objects as 130 nm high Si nanopillars with average diameters of 35 nm prepared on top of a Si wafer at an areal density of 127 μm^{-2} can reliably be imaged by freeze fracture in combination with SEM in BSE mode. Both W- as well as CB-states could be distinguished and the three-phase lines liquid–solid–air made visible.

It turned out that the applied combination of rapid freezing at 77 K and *in situ* coating of the ice replica by thin C- and Pt-layers not only suppressed water crystallization and related surface roughening of the replica but also stabilized its surface during SEM analysis by avoidance of charging and heating effects. Furthermore, by evaporating the Pt layer under 45°, the resulting dark/bright contrast of indentations provided additional quantitative depth information. Alltogether, for the periodically arranged pillar indentations, a contrast resolution of approximately 5 nm could be accomplished.

Due to the rapid freezing of water, however, triggering shock waves leading to uncontrolled local pressure enhancements, the imaged wetting states do not generally represent equilibrium states. This could be demonstrated on a nanopatterned Si surface which according to CA hysteresis measurements was clearly in a stable CB-state forming a superhydrophobic surface. Nevertheless, after freeze fracture, the SEM analyzed replica revealed the simultaneous presence of both CB- and W-states, with the W-state preferentially but not exclusively penetrating

the CB-state from the outer periphery of the nanopatterned area or at defects like missing nanopillars.

From a wetting point of view, the observed lateral sharpness of the boundary between coexisting CB- and W-states extending only one nanopillar distance, that is, approximately 90 nm, is remarkable. This leads to the conclusion that saddle-shaped zero-curvature surfaces are possible even on the nanoscale.

ASSOCIATED CONTENT

S Supporting Information

Movies of bouncing droplet on superhydrophobic and nonbouncing droplet on flat surface; additional information for imaging in BSE-mode. This material is available free of charge via the Internet at <http://pubs.acs.org>.

AUTHOR INFORMATION

Notes

The authors declare no competing financial interest.

ACKNOWLEDGMENTS

We thank the Collaborative Research Center, SFB 569, of the German Science Foundation as well as Network of Functional Nanostructures, BW-Stiftung, for financial support. For help with the micellar solutions and dip-coating, we thank Axel Seidenstücker, Burcin Özdemir, and Stephan Kleinert.

REFERENCES

- (1) Barthlott, W.; Neinhuis, C. Purity of the sacred lotus, or escape from the contamination in biological surfaces. *Planta* **1997**, *202*, 1–8.
- (2) Patankar, N. A. Mimicking the Lotus Effect: Influence of Double Roughness Structures and Slender Pillars. *Langmuir* **2004**, *20*, 8209–80213.
- (3) Quere, D. Wetting and Roughness. *Annu. Rev. Mater. Res.* **2008**, *38*, 71–99.
- (4) Rykaczewski, K.; Scott, J. H. J. Methodology for Imaging Nano- to Microscale Water Condensation Dynamics on Complex Nanostructures. *ACS Nano* **2011**, *5*, 5962–5968.
- (5) Liu, M.; Zheng, Y.; Zhai, J.; Jiang, L. Bioinspired Super-antiwetting Interfaces with Sessile Liquid-Solid Adhesion. *Acc. Chem. Res.* **2010**, *43*, 368–377.
- (6) Nosonovsky, M.; Bhushan, B. Biologically Inspired Surfaces: Broadening the Scope of Roughness. *Adv. Funct. Mater.* **2008**, *18*, 843–855.
- (7) Bormashenko, E. Wetting transitions on biomimetic surfaces. *Phil. Trans. R. Soc. A* **2010**, *368*, 4695–4711.
- (8) Ensikat, H. J.; Schulte, A. J.; Koch, K.; Barthlott, W. Droplets on Superhydrophobic Surfaces: Visualization of the Contact Area by Cryo-Scanning Electron Microscopy. *Langmuir* **2009**, *25*, 13077–13083.

- (9) Miljkovic, N.; Enright, R.; Wang, E. N. Effect of Droplet Morphology on Growth Dynamics and Heat Transfer during Condensation on Superhydrophobic Nanostructured Surfaces. *ACS Nano* **2012**, *6*, 1776–1785.
- (10) Liu, K.; Yao, X.; Jiang, L. Recent developments in bio-inspired special wettability. *Chem. Soc. Rev.* **2010**, *39*, 3240–3255.
- (11) Dorrer, C.; Rühe, J. Micro to nano: Surface size scale and superhydrophobicity. *Beilstein J. Nanotechnol.* **2011**, *2*, 327–332.
- (12) Ensikat, H. J.; Ditsche-Kuru, P.; Neinhuis, C.; Barthlott, W. Superhydrophobicity in perfection: the outstanding properties of the lotus leaf. *Beilstein J. Nanotechnol.* **2011**, *2*, 152–161.
- (13) Lau, K. K. S.; Bico, J.; Teo, K. B. K.; Chhowalla, M.; Amarasingha, G. A. J.; Milne, W. I.; McKinley, G. H.; Gleason, K. K. Superhydrophobic Carbon Nanotube Forests. *Nano Lett.* **2003**, *3*, 1701–1705.
- (14) Wenzel, R. N. Resistance of solid surfaces to wetting by water. *Ind. Eng. Chem.* **1936**, *28*, 988–994.
- (15) Cassie, A. B. D.; Baxter, S. Wettability of porous surfaces. *Trans. Faraday Soc.* **1944**, *40*, 546–551.
- (16) Bico, J.; Marzolin, C.; Quere, D. Pearl drops. *Europhys. Lett.* **1999**, *47* (2), 220–226.
- (17) Yeh, K.-Y.; Chen, L.-J.; Chang, J.-Y. Contact Angle Hysteresis on Regular Pillar-like Hydrophobic Surfaces. *Langmuir* **2008**, *24*, 245–251.
- (18) Moulinet, S.; Bartolo, D. Life and death of a fakir droplet: Impalement transitions on superhydrophobic surfaces. *Eur. Phys. J. E* **2007**, *24*, 251–260.
- (19) Sbragaglia, M.; Peters, A. M.; Pirat, C.; Borkent, B. M.; Lammertink, R. G. H.; Wessling, M.; Lohse, D. Spontaneous Breakdown of Superhydrophobicity. *Phys. Rev. Lett.* **2007**, *99* (156001), 1–4.
- (20) Rathgen, H.; Mugele, F. Microscopic shape and contact angle measurement at a superhydrophobic surface. *Faraday Discuss.* **2010**, *146*, 49–56.
- (21) Bartolo, D.; Bouamrane, F.; Verneuil, E.; Buguin, A.; Silberzan, P.; Moulinet, S. Bouncing or sticky droplets: Impalement transitions on superhydrophobic micropatterned surfaces. *Europhys. Lett.* **2006**, *74*, 299–305.
- (22) Martines, E.; Seunarine, K.; Morgan, H.; Gadegaard, N.; Wilkinson, C. D. W.; Riehle, M. O. Superhydrophobicity and Superhydrophilicity of Regular Nanopatterns. *Nano Lett.* **2005**, *5*, 2097–2103.
- (23) Walther, P.; Wehrli, E.; Hermann, R.; Müller, M. Double-layer coating for high-resolution low-temperature scanning electron microscopy. *J. Microsc.* **1995**, *179*, 229–237.
- (24) Wu, A. H. F.; Cho, K. L.; Liaw, I. L.; Moran, G.; Kirby, N.; Lamb, R. N. Hierarchical surfaces: an *in situ* investigation into nano and micro scale wettability. *Faraday Discuss.* **2010**, *146*, 223–232.
- (25) Isa, L.; Lucas, F.; Wepf, R.; Reimhult, E. Measuring single-nanoparticle wetting properties by freeze-fracture shadow-casting cryo-scanning electron microscopy. *Nat. Commun.* **2011**, *2*, 438 (9).
- (26) Spatz, J. P.; Mössmer, S.; Hartmann, C.; Möller, M.; Herzog, T.; Krieger, M.; Boyen, H.-G.; Ziemann, P.; Kabius, B. Ordered Deposition of Inorganic Clusters from Micellar Block Copolymer Films. *Langmuir* **2000**, *16*, 407–415.
- (27) Härtling, T.; Seidenstücker, A.; Olk, P.; Plettl, A.; Ziemann, P.; Eng, L. M. Ordered photochemical particle growth in two-dimensional ordered metal nanoparticle arrays. *Nanotechnology* **2010**, *21*, 145309 (6).
- (28) Manzke, A.; Pfahler, C.; Dubbers, O.; Plettl, A.; Ziemann, P.; Crespy, D.; Schreiber, E.; Ziener, U.; Landfester, K. Etching Masks based on Miniemulsions: A Novel Route towards Ordered Arrays of Surface Nanostructures. *Adv. Mater.* **2007**, *19*, 1337–1341.
- (29) Walther, P. Recent progress in freeze-fracturing of high-pressure frozen samples. *J. Microsc.* **2003**, *212*, 34–43.
- (30) Kwon, H. M.; Paxson, A. T.; Varanasi, K. K.; Patankar, N. A. Rapid Deceleration-Driven Wetting Transition during Pendant Drop Deposition on Superhydrophobic Surfaces. *Phys. Rev. Lett.* **2011**, *106*, 036102 (4).
- (31) Bauerecker, S.; Ulbig, P.; Buch, V.; Vrbka, L.; Jungwirth, P. Monitoring Ice Nucleation in Pure and Salty Water via High-Speed Imaging and Computer Simulations. *J. Phys. Chem. C* **2008**, *112*, 7631–7636.
- (32) Deng, T.; Varanasi, K. K.; Ming, H.; Bhate, N.; Keimel, C.; Stein, J.; Blohm, M. Nonwetting of impinging droplets on textured surfaces. *Appl. Phys. Lett.* **2009**, 133109.